Energy & Environmental Science

ROYAL SOCIETY OF CHEMISTRY

PAPER

View Article Online
View Journal | View Issue

Cite this: *Energy Environ. Sci.*, 2024, **17**, 2018

Enhanced average power factor and *ZT* value in PbSe thermoelectric material with dual interstitial doping†

Liqing Xu,[ab] Xiaoying Wang,[b] Yang Wang,[b] Zhibin Gao,[b] Xiangdong Ding[b] and Yu Xiao *[a]

Received 27th December 2023,
Accepted 30th January 2024

DOI: 10.1039/d3ee04539k

rsc.li/ees

Thermoelectric materials necessitate both high power factors and *ZT* values in practical applications, as they determine the output power and conversion efficiency, respectively. However, the average power factor is often suppressed when structural defects are imported to pursue a high-ranged *ZT* value. In this work, a high average power factor of 24.18 μW cm^{-1} K^{-2} and an average *ZT* value of 1.01 at 300–773 K are simultaneously achieved for n-type $Pb_{1.02}Se$–0.2%Cu through dual interstitial doping, which surpasses other low-cost Se/S-based n-type thermoelectric materials. Its exceptional thermoelectric performance primarily stems from decoupled carrier and phonon transport properties induced by Pb and Cu dual interstitials. Firstly, Pb and Cu dual interstitials in n-type $Pb_{1.02}Se$–0.2%Cu can fully optimize temperature-dependent carrier density from 1.27 × 10^{19} cm^{-3} at 300 K to 3.90 × 10^{19} cm^{-3} at 773 K, thus maximizing the power factor to 32.83 μW cm^{-1} K^{-2} and resulting in an average power factor of 24.18 μW cm^{-1} K^{-2}. Additionally, Pb and Cu dual interstitials cause electron-dominated hierarchical defects (cation interstitials, Se vacancies, dislocations and Pb precipitates), which can significantly reduce lattice thermal conductivity while preserving high electrical transport properties. As a result of the optimized electrical and thermal transport properties, the thermoelectric performance of n-type $Pb_{1.02}Se$–0.2%Cu is largely enhanced over a wide range of temperatures.

Broader context

With environmental pollution and global warming being critical concerns, thermoelectric technology based on the Seebeck effect has demonstrated large potential for directly converting thermal energy into electrical energy without any harmful emissions. Thermoelectric efficiency and output power are respectively determined by the *ZT* values and power factors of thermoelectric materials. However, it is challenging to simultaneously achieve a high average power factor and *ZT* value, especially when structural defects are imported to pursue a high-ranged *ZT* value, due to the interplay among thermoelectric parameters. To improve the practical thermoelectric efficiency and output power, this work introduces a novel strategy of dual interstitial doping to enhance both the average power factor and *ZT* value of the PbSe thermoelectric material. As a result, both a high average power factor of 24.18 μW cm^{-1} K^{-2} and an average *ZT* value of 1.01 at 300–773 K are achieved for n-type $Pb_{1.02}Se$–0.2%Cu through dual Pb and Cu interstitial doping, which benefits from the fully optimized temperature-dependent carrier density and electron-dominated defect regions to decouple the phonon and carrier transport. This high-performance $Pb_{1.02}Se$–0.2%Cu thermoelectric material not only obviously exceeds previous single interstitial doped n-type PbSe samples, but also shows a strong competitive advantage over other low-cost Se/S-based (Te free) n-type thermoelectric materials. This work proves the feasibility of dual interstitials in effectively decoupling carrier and phonon transport and also could inspire more strategies of dual or multiple interstitial doping to be extended to other thermoelectric materials.

Introduction

Thermoelectric technology enables direct conversion between heat and electricity based on the Seebeck effect and Peltier effect, which can be applied in waste heat utilization and thermoelectric refrigeration.[1–3] The energy conversion efficiency of thermoelectric technology is mainly related to thermoelectric materials and it is characterized by the dimensionless figure of merit (*ZT*), $ZT = S^2\sigma T/(\kappa_{ele} + \kappa_{lat})$, where S, σ, T, κ_{ele} and

[a] *School of Materials and Energy, University of Electronic Science and Technology of China, Chengdu 611731, China. E-mail: xiaoyu@uestc.edu.cn*
[b] *State Key Laboratory for Mechanical Behavior of Materials, Xi'an Jiaotong University, Xi'an 710049, China*

† Electronic supplementary information (ESI) available. See DOI: https://doi.org/10.1039/d3ee04539k

κ_{lat} denote the Seebeck coefficient, electrical conductivity, absolute temperature in kelvin, electronic thermal conductivity and lattice thermal conductivity, respectively. As is widely known, the strong coupling between electrical and thermal transport properties poses a challenge in achieving a high ZT value. Indeed, practical thermoelectric materials must possess both high power factors ($S^2\sigma$) and ZT values, as they respectively determine the output power and conversion efficiency.[4–7] In addition, the developed strategies still face difficulties in achieving both a high power factor and ZT value, such as band structure manipulation[8–10] and nanostructure engineering.[11–13]

It is reported that the strategy of interstitial doping in thermoelectric materials can synergistically optimize electrical and thermal transport properties and even decouple the carrier and phonon transport due to their large different mean free paths.[14,15] In PbQ (Q = Te, Se and S) compounds, Zn,[16,17] Ni,[17,18] Cu[19–21] and Ag[22] atoms can form interstitials in the matrix lattice. These sub-nanoscale interstitials could intensify the phonon scattering to decrease lattice thermal conductivity due to the comparable size with the phonon mean free path, while simultaneously maintaining carrier transport because of a much larger carrier mean free path. Additionally, interstitials play multiple roles in optimizing thermoelectric performance, which have also been proved in other materials. Interstitial doping elements, such as Yb,[23] In,[24] Ce[25] and Br,[26] can fill the icosahedral voids in skutterudite to form rattling atoms, thus blocking phonon transport and suppressing lattice thermal conductivity. Ni or Cu interstitials in half-Heusler compounds can regulate carrier density and simultaneously produce point defects to scatter phonon transport.[27–29] Besides, Cu interstitial doping in half-Heusler compounds can induce wetting layers between grains and form coherent grain boundaries to optimize carrier transport properties.[29] In Bi_2Q_3 (Q = Te, Se and S) compounds, Cu and Ag interstitial atoms can enter into the layer gap and accelerate the electron transport across the layers, thus enhancing the electrical transport properties.[30–34] A similar carrier transport phenomenon has also been found in a layered $SnSe_2$ compound with Cu or Ag interstitial doping.[35–37] Notably, different from using nanostructures to cause strong carrier scattering, interstitials are promising to achieve both high power factors and ZT values. Moreover, the significant role of interstitials discussed above serves as an inspiration to further investigate strategies involving dual interstitial or multiple interstitial doping in thermoelectric materials.

This work reports a low-cost PbSe thermoelectric material to demonstrate the feasibility of dual interstitial doping in decoupling thermoelectric parameters. Pb and Cu atoms are selected as dual interstitial dopants to firstly compensate the intrinsic Pb vacancies and subsequently produce massive interstitials in the stoichiometric PbSe compound, which can dynamically optimize the temperature-dependent carrier density. The synergy of Pb and Cu interstitial doping in n-type $Pb_{1.02}Se$–0.2%Cu can tune the carrier density to an optimal range, from 1.27×10^{19} cm^{-3} at 300 K to 3.90×10^{19} cm^{-3} at 773 K. The dynamically optimized carrier density in n-type $Pb_{1.02}Se$–0.2%Cu with dual interstitial doping leads to a high average power factor of 24.18 μW cm^{-1} K^{-2} over a wide range of temperatures (300–773 K), which is obviously larger than that of the Pb or Cu single interstitial doped sample and even surpasses those of other low-cost Se/S-based n-type thermoelectric materials. Furthermore, the theoretical calculation and microstructure observation unclose hierarchical defects in $Pb_{1.02}Se$–0.2%Cu, including sub-nanoscale Pb and Cu interstitials, Se vacancies, dislocations and some nanoscale Pb precipitates, and these electron-dominated defects can preserve high electron transport but impede phonon propagation. As a result, the ZT_{ave} value enhances from 0.46 in $Pb_{1.02}Se$ and 0.91 in PbSe–0.2%Cu to 1.01 in $Pb_{1.02}Se$–0.2%Cu at 300–773 K. The remarkable average power factor and average ZT value observed for $Pb_{1.02}Se$–0.2%Cu highlight significant advancements compared to other low-cost Se/S-based n-type thermoelectric materials.

Results and discussion

Enhanced thermoelectric performance of $Pb_{1.02}Se$–0.2%Cu

The strategy of dual interstitial doping is introduced in the n-type PbSe thermoelectric material by selecting Pb and Cu, which can firstly fill intrinsic Pb vacancies in stoichiometric PbSe and then induce massive interstitials to optimize electrical transport properties. Notably, Pb and Cu dual interstitial doping in n-type $Pb_{1.02}Se$–0.2%Cu contributes to its superior thermoelectric performance compared with those of other n-type PbSe samples optimized by single interstitial doping, as shown in Fig. 1. A maximum room-temperature PF value of 32.83 μW cm^{-1} K^{-2} can be obtained for n-type $Pb_{1.02}Se$–0.2%Cu, which exceeds those of other n-type PbSe samples with single interstitial doping, including 21.85 μW cm^{-1} K^{-2} for PbSe–4%Pb,[38] 26.69 μW cm^{-1} K^{-2} for $PbSe_{0.996}$,[39] 23.72 μW cm^{-1} K^{-2} for $PbCu_{0.00125}Se$,[20] and 19.91 μW cm^{-1} K^{-2} for $PbZn_{0.0125}Se$,[16] as shown in Fig. 1(a). In this work, the room-temperature PF value increases from 25.18 μW cm^{-1} K^{-2} for $Pb_{1.02}Se$ and 28.14 μW cm^{-1} K^{-2} for PbSe–0.2%Cu to 32.83 μW cm^{-1} K^{-2} for $Pb_{1.02}Se$–0.2%Cu. Such a high room-temperature PF value of $Pb_{1.02}Se$–0.2%Cu stems from its suitable carrier density tuned by Pb and Cu dual interstitial doping, which finally contributes to an enhanced room-temperature ZT value of 0.54, as shown in Fig. 1(b).

Both the electrical conductivity (σ) and Seebeck coefficient (S) are closely related to carrier density. Therefore, the optimized carrier density in $Pb_{1.02}Se$–0.2%Cu with Pb and Cu dual interstitial doping can tune these two thermoelectric parameters (σ and S) to an optimal range, thus resulting in a large PF (PF = $S^2\sigma$) value shown in Fig. 1(c). Moreover, the well optimized electrical conductivity and Seebeck coefficient of $Pb_{1.02}Se$–0.2%Cu not only enhance the near-room-temperature PF (PF_{RT}) value, but also obviously boost the average PF (PF_{ave}) value and average ZT (ZT_{ave}) value to 24.18 μW cm^{-1} K^{-2} and 1.01 at 300–773 K, as shown in Fig. S1 (ESI†). Compared with other n-type PbSe materials with single interstitial doping, $Pb_{1.02}Se$–0.2%Cu presents much higher values of both PF_{ave} and

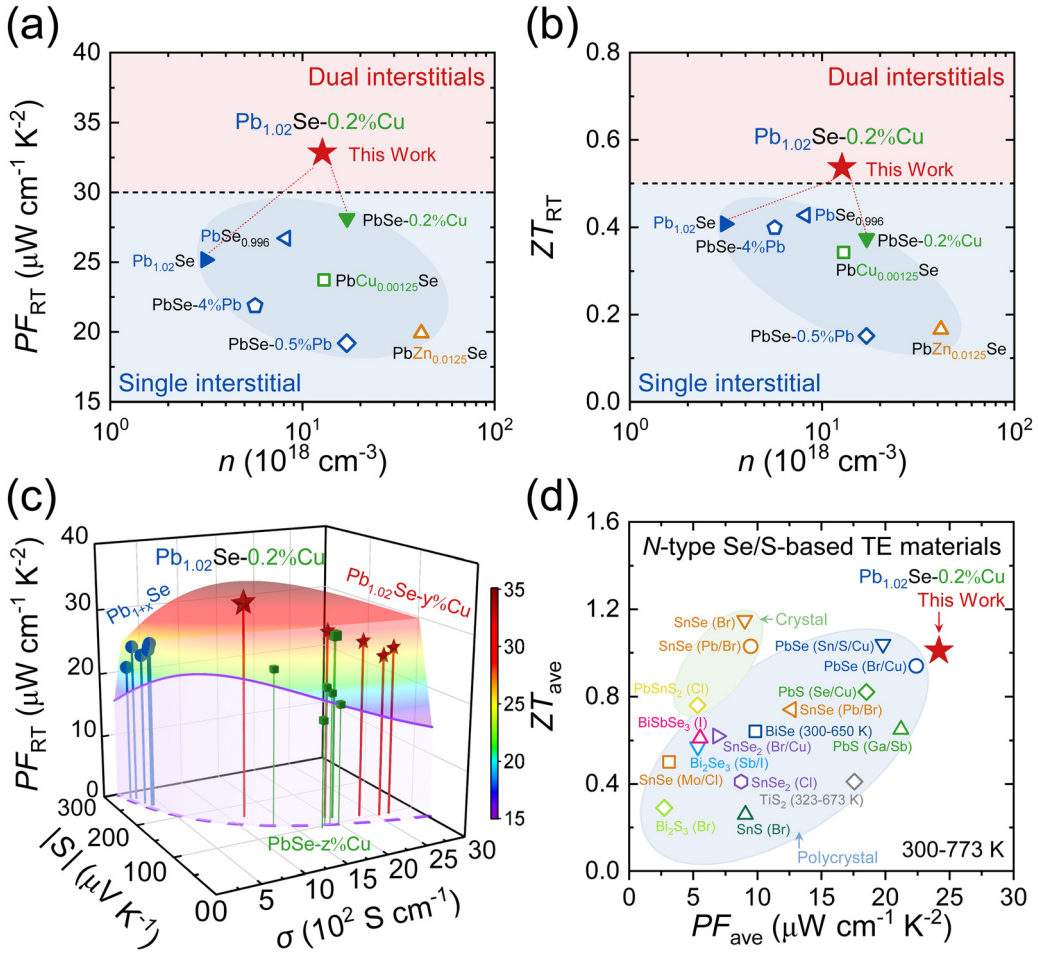

Fig. 1 Comparison of thermoelectric performance as a function of carrier density in n-type PbSe thermoelectric materials with interstitial doping: (a) PF value; (b) ZT value; (c) the room-temperature PF value as a function of S and σ; (d) comparison of the ZT_{ave} value and the PF_{ave} value with those of other n-type low-cost Se/S-based (Te free) thermoelectric materials, including crystals: SnSe (Br),[40] SnSe (Pb/Br),[41] and $PbSnS_2$ (Cl)[42] and polycrystals: PbSe (Sn/S/Cu),[8] PbSe (Br/C),[43] PbS (Se/Cu),[44] PbS (Ga/Sb),[10] SnSe (Pb/Br),[45] SnSe (Mo/Cl),[46] $SnSe_2$ (Br/Cu),[47] $SnSe_2$ (Cl),[48] SnS (Br),[49] BiSe,[50] Bi_2Se_3 (Sb/I),[51] $BiSbSe_3$ (I),[52] Bi_2S_3 (Br),[53] and TiS_2.[54]

ZT_{ave} over a wide range of temperatures, indicating the great advantages of the dual interstitial doping strategy. Furthermore, compared with other low-cost Se/S-based (Te free) n-type thermoelectric materials, $Pb_{1.02}Se$–0.2%Cu shows an obviously enhanced PF_{ave}, even much higher than that of the n-type SnSe crystals,[40,41] and it can simultaneously maintain a comparably high ZT_{ave} value at 300–773 K, as shown in Fig. 1(d). The coexistence of high PF_{ave} and ZT_{ave} values for low-cost $Pb_{1.02}Se$–0.2%Cu can enable simultaneous improvements in output power and conversion efficiency, thus making it a competitive candidate for practical thermoelectric power generation in the low to medium temperature range.

Electrical transport properties

In this work, we firstly prepared n-type PbSe samples with single Pb interstitial doping, $Pb_{1+x}Se$ (x = 0.005–0.03), and then introduced the Cu interstitial dopant into the optimum $Pb_{1.02}Se$ component to work as the dual interstitial dopant. The powder X-ray diffraction (PXRD) patterns of $Pb_{1+x}Se$ (x = 0.005–0.03) and $Pb_{1.02}Se$–y%Cu (y = 0.0–1.0) are shown in Fig. S2 (ESI†). The thermoelectric performances and sample densities of $Pb_{1+x}Se$ (x = 0.005–0.03) and $Pb_{1.02}Se$–y%Cu (y = 0.0–1.0) are presented in Fig. S3–S7 and Table S1 (ESI†), and the optimal contents are picked out to make a comparison. Although the extra Pb phase can be observed in the Pb interstitial doped PbSe matrix, the expanded lattice parameter and increased carrier density shown in Fig. S8 (ESI†) can prove that part of the Pb and Cu atoms indeed successfully enter into interstitial sites in the PbSe lattice, which can favorably tune the electron transport properties of n-type PbSe thermoelectric materials.

The temperature-dependent electrical transport properties of n-type $Pb_{1.02}Se$, PbSe–0.2%Cu and $Pb_{1.02}Se$–0.2%Cu samples are compared in Fig. 2. As shown in Fig. 2(a), $Pb_{1.02}Se$–0.2%Cu exhibits medium electrical conductivity in a low temperature range (300–600 K), which exceeds the values of $Pb_{1.02}Se$ and PbSe–0.2%Cu at high temperatures (600–773 K), obviously showing dynamically tuned electrical transport properties.

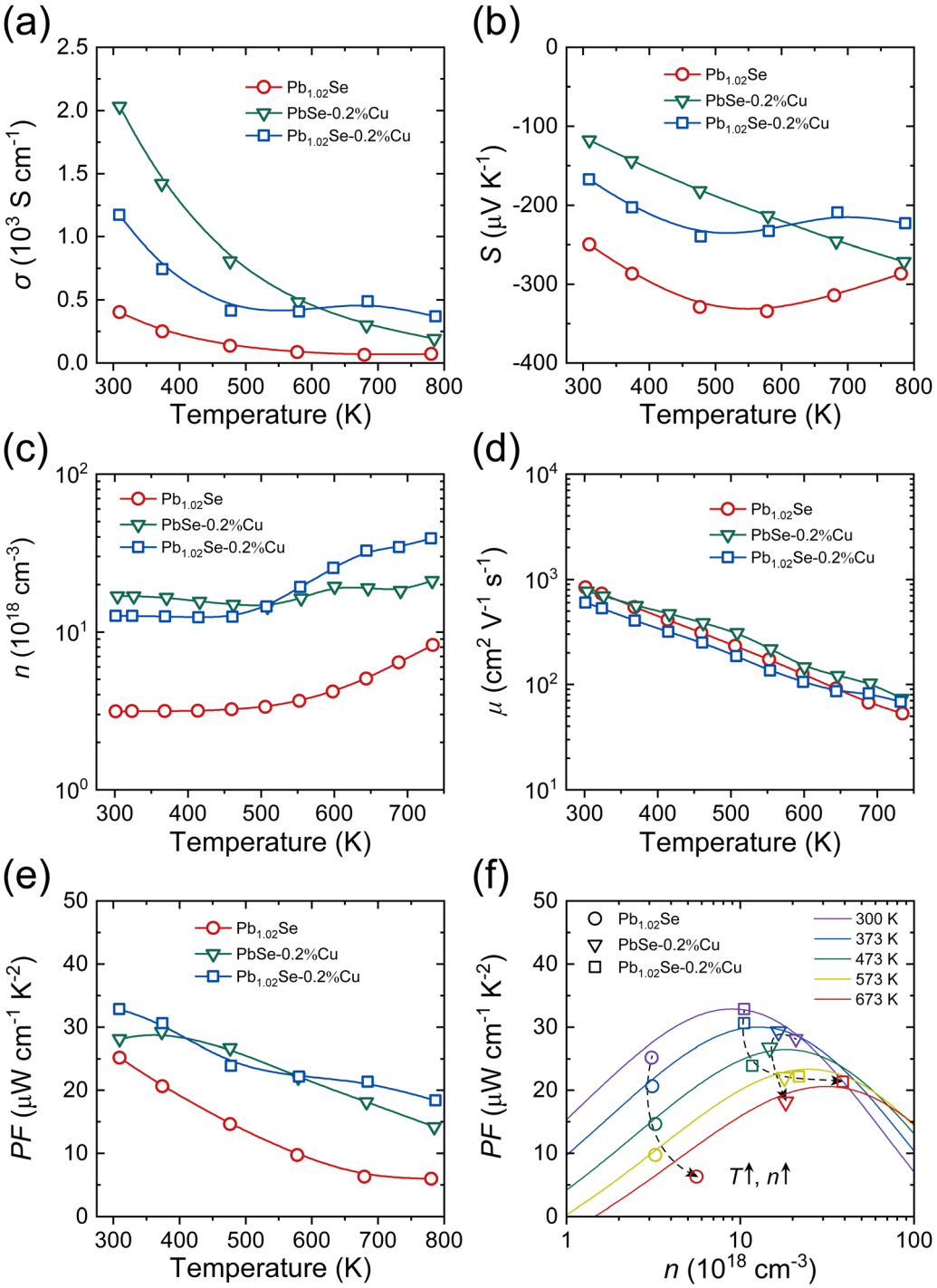

Fig. 2 Temperature-dependent electrical transport properties of $Pb_{1.02}Se$, PbSe–0.2%Cu and $Pb_{1.02}Se$–0.2%Cu: (a) electrical conductivity; (b) Seebeck coefficient; (c) carrier density; (d) carrier mobility; (e) PF value, and (f) experimentally and theoretically calculated PF values as a function of carrier density.

In addition, the temperature-dependent Seebeck coefficient in Fig. 2(b) shows the same tendency as electrical conductivity. To unveil these special electrical transport properties of Pb and Cu interstitial-doped PbSe samples, temperature-dependent carrier density and carrier mobility are measured. Both $Pb_{1.02}Se$ and PbSe–0.2%Cu samples with single interstitial doping present dynamic carrier density optimization such that the carrier density continuously increases with rising temperature, as shown in Fig. 2(c). This dynamic optimization of carrier density arises from the increasing solubility of the Cu or Pb interstitial in the PbSe matrix when temperature rises, and the Cu or Pb interstitial will release extra free electrons into the matrix to amplify the carrier density.[20,21,55] It is shown that $Pb_{1.02}Se$ has a smaller carrier density than PbSe–0.2%Cu in the whole

temperature range, indicating a lower interstitial solubility of Pb in the PbSe matrix, which is caused by the larger atomic radius of the Pb atom (1.75 Å) than the Cu atom (1.28 Å). Obviously, the Pb interstitial in the PbSe matrix can cause strong lattice distortion and reversely suppress the Cu solubility, thus lowering the carrier density in $Pb_{1.02}Se$–0.2%Cu at 300–523 K compared with PbSe–0.2%Cu. As the temperature increases, the lattice of the PbSe matrix undergoes continuous expansion, thus leading to an increase in the solubility of both Pb and Cu interstitials. As a result, the carrier density at high temperature (above 523 K) can be largely improved in dual Pb and Cu interstitial doped $Pb_{1.02}Se$–0.2%Cu. In addition, the carrier density in n-type $Pb_{1.02}Se$–0.2%Cu is fully optimized in a large range from 1.27×10^{19} cm^{-3} at 300 K to 3.90×10^{19} cm^{-3} at 773 K due to interplay effects of Pb and Cu interstitials. Fig. 2(d) shows the temperature-dependent carrier mobility, and all the interstitial doped PbSe materials can preserve high carrier mobility, thus leading to excellent electrical transport properties.

Fig. 2(e) shows the PF value of $Pb_{1.02}Se$, PbSe–0.2%Cu and $Pb_{1.02}Se$–0.2%Cu samples. It is seen that $Pb_{1.02}Se$–0.2%Cu with dual interstitial doping has an obviously higher PF value compared with $Pb_{1.02}Se$ and PbSe–0.2%Cu with single interstitial doping. To further unclose the relationship between carrier density and the PF value, theoretical calculations are presented based on the single Kane band (SKB) model and the electrical transport coefficients can be written as follows:

Hall carrier density

$$n_H = R_H^{-1}\frac{(2m^*k_BT)^{3/2}}{2\pi\hbar^3}{}^0F_0^{3/2} \quad (1)$$

Hall factor

$$R_H = \frac{3K(K+2)}{(2K+1)^2}\frac{{}^0F_{-4}^{1/2}\,{}^0F_0^{3/2}}{\left({}^0F_{-2}^1\right)^2} \quad (2)$$

Hall carrier mobility

$$\mu_H = R_H\frac{2\pi\hbar^4eC_l}{m_I^*\left(2m_b^*k_BT\right)^{3/2}E_{def}{}^2}\frac{3\,{}^0F_{-2}^1}{{}^0F_0^{3/2}} \quad (3)$$

Seebeck coefficient

$$S = \frac{k_B}{e}\left(\frac{{}^1F_{-2}^1}{{}^0F_{-2}^1} - \xi\right) \quad (4)$$

Fermi integral

$${}^nF_k^m = \int_0^\infty\left(-\frac{\partial f}{\partial\varepsilon}\right)\varepsilon^n\left(\varepsilon+\alpha\varepsilon^2\right)^m\left[(1+2\alpha\varepsilon)^2+2\right]^{k/2}d\varepsilon \quad (5)$$

Power factor

$$PF = \frac{2N_V\hbar k_B{}^2C_l}{\pi E_{def}{}^2}\frac{1}{m_I^*}\left(\frac{{}^1F_{-2}^1}{{}^0F_{-2}^1} - \xi\right)^2{}^0F_{-2}^1 \quad (6)$$

where k_B, $\hbar$ and e represent the Boltzmann constant, reduced Planck constant and unit charge, respectively. The density of states effective mass $m^* = m_b^*(N_V)^{3/2}$, band effective mass $m_b^* = (m_\perp^{*2}+m_\parallel^*)^{1/3}$, parameter $K = m_\parallel^*/m_\perp^*$, reduced band gap $\alpha = k_BT/E_g$, Fermi–Dirac distribution function $f = 1/[1 + \exp(\varepsilon - \xi)]$, and reduced Fermi level $\xi = E_F/k_BT$, where E_F is the Fermi level. For the PbSe thermoelectric material, the variable constants band degeneracy $N_V = 4$, longitudinal effective mass $m_\parallel^* \approx 0.7m_e$, transverse effective mass $m_\perp^* \approx 0.4m_e$,[56] average longitudinal elastic modulus $C_l \approx 9.1 \times 10^{10}$ Pa,[57] band gap $E_g \approx 0.29$ eV and deformation potential coefficient $E_{def} \approx 25$ eV.[58] The calculation results in Fig. 2(f) show that the theoretical maximum power factor of n-type PbSe requires an optimal dynamic optimization of carrier density in the whole temperature range. Owing to the fully optimized temperature-dependent carrier density in Pb and Cu dual interstitial doped $Pb_{1.02}Se$–0.2%Cu, its experimental PF value can well match the theoretical value, thus leading to a high PF_{ave} value over a wide range of temperatures.

Theoretical charge density

Theoretical charge density and local electron density are employed to investigate the bonding environment that has a close relationship with electrical transport properties. According to the defect formation calculation results in Fig. S9 (ESI†), the Cu interstitial (Cu_i), the Pb interstitial (Pb_i) and Se vacancies (V_{Se}) have low formation energies in the $Pb_{1.02}Se$–0.2%Cu sample under Pb-rich conditions. Thus, the density functional theory (DFT) calculation is implemented with these defects in this work to analyse the effect of Pb and Cu dual interstitial doping on the carrier transport properties of $Pb_{1.02}Se$–0.2%Cu.

Fig. 3(a) and (b) shows the 2D iso-surface representation of the calculated charge density within the (10−1) plane in undoped PbSe and $Pb_{1.02}Se$–0.2%Cu. The charge density analysis shows the transfer of electrons among Pb, Se, and Cu atoms, where the red and blue colors mean the large accumulation and depletion regions of charge, respectively. As shown in Fig. 3(b), both the Pb interstitial and the Cu interstitial can produce overlapping electron clouds with the matrix to form broad charge channels, which significantly facilitate the charge transfer and could benefit high carrier transport properties. Moreover, a larger range of overlapping electron clouds induced by the Cu interstitial than that by the Pb interstitial can be clearly observed in the 3D iso-surface charge density, shown in Fig. 3(c) and (d), which result in the superior electrical conductivity of PbSe–0.2%Cu compared to that of $Pb_{1.02}Se$. Se vacancies in Fig. 3(e) cause deficiency of charge density, but it can theoretically provide two free electrons to the PbSe matrix. Therefore, all these Cu_i, Pb_i and V_{Se} are intrinsic electron-dominated defects, and they could play favorable roles in electron transport in n-type $Pb_{1.02}Se$–0.2%Cu. Additionally, the electron localization function (ELF) provides a yardstick for the degree of electron localization.[59] Fig. S10 (ESI†) shows the ELF map of the Pb interstitial, the Cu interstitial and Se vacancy, and the value lies between 0 and 1. ELF = 1 indicates that the electrons are perfectly localized, while ELF = 0.5 suggests homogeneous electron gas.[60,61] An ELF value of 0.2 around the Cu interstitial is very low, which signifies that the electrons around the Cu interstitial are easily delocalized.

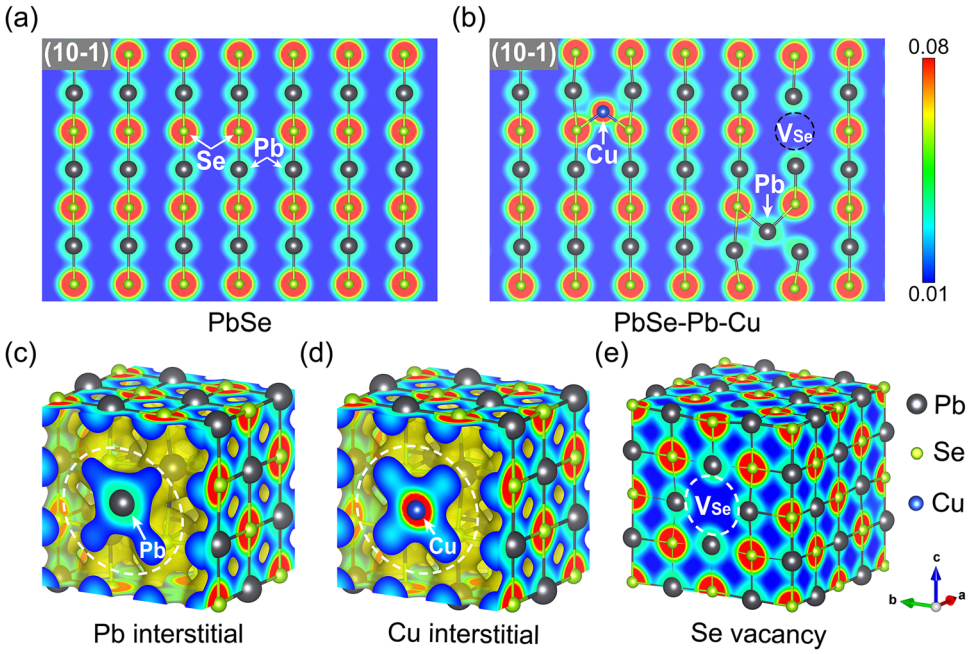

Fig. 3 Theoretical charge densities (in units of e bohr^{-3}) of PbSe and $Pb_{1.02}Se$–0.2%Cu: (a) 2D charge density of undoped PbSe without defects; (b) 2D charge density of $Pb_{1.02}Se$–0.2%Cu with defects of the Pb interstitial, the Cu interstitial and Se vacancy. 3D iso-surface charge density around (c) the Pb interstitial, (d) the Cu interstitial and (e) Se vacancy.

The Pb interstitial has an ELF value of above 0.5 with high electron localization, but the electrons around the Pb interstitial can also be partly delocalized to participate in carrier transport. As a result, both theoretical charge density and the electron localization function confirm that Pb and Cu dual interstitials can benefit the high carrier transport properties of n-type $Pb_{1.02}Se$–0.2%Cu.

Microstructure observations

The microstructure of Pb and Cu dual interstitial doped $Pb_{1.02}Se$–0.2%Cu is observed by Cs-corrected transmission electron microscopy and also compared with those of undoped PbSe sample. Fig. 4(a) shows the annular bright field (ABF)-STEM morphological image of $Pb_{1.02}Se$–0.2%Cu, revealing the presence of some ellipsoidal nanoprecipitates and dislocation lines. In order to identify the composition, the EDS analysis is conducted and the results are depicted in Fig. 4(b1–4). Fig. 4(b1) is a magnified image of the nanoprecipitate captured in Fig. 4(a). It can be observed that the Pb element is enriched in the precipitate area, and the precipitate size is approximately several hundred nanometers. Fig. 4(c) displays an enlarged ABF-STEM image of the other regions shown in Fig. 4(a), and numerous dislocations can be evidently observed, while the stoichiometric PbSe sample has scarce dislocation lines, but a large number of Pb vacancies, as shown in Fig. S11 (ESI†). Thus, it can be concluded that the Pb interstitial doping can effectively fill the Pb vacancies and the dislocations in $Pb_{1.02}Se$–0.2%Cu mainly arise from Pb and Cu dual interstitial doping.

Fig. 4(d) shows the high angle annular dark field (HAADF)-STEM image at the atomic level, where it is clear that some interstitial atoms are present in the middle part of the image. Additionally, Fig. 4(e) displays an enlarged image of Fig. 4(d) with the observed direction along the [110] axis. As the contrast of the HAADF image is proportional to the atomic number, it enables a clear distinction between brighter Pb (atomic number 82) and darker Se (atomic number 34) atoms. The presence of Pb interstitial atoms is confirmed by the line profile along the red dashed line in the inset of Fig. 4(e), because clear interstitial atoms have the same intensity as Pb atoms. A typical atomic image of the dislocation region is displayed in Fig. 4(f), while Fig. 4(i) shows an inverse fast Fourier transform (IFFT) image that provides a clearer depiction of the dislocation lines. Fig. 4(g) and (h) and Fig. S12 (ESI†) demonstrate the HAADF-STEM image of the interstitial Cu atom region. The presence of interstitial atoms in the marked lattice site (labeled with a white box) is indicated in Fig. 4(h). Due to the principle of *Z*-contrast and the atomic number of Cu being 29, its contrast is expected to be close to that of Se atoms, but much darker than the Pb atoms. Additionally, the smaller atomic size of Cu enables it to be clearly distinguished from the interstitial Pb atoms observed in Fig. 4(e). Consequently, it can be determined that the interstitial atoms indicated by the red arrows in Fig. 4(h) represent the Cu interstitial in the PbSe matrix. Thus, the introduction of additional Pb and Cu results in a large number of Pb nanoprecipitates, dislocations, and interstitial Pb and Cu atoms in the $Pb_{1.02}Se$–0.2%Cu sample. In addition, these hierarchical defects can block the phonon transport, thus largely decreasing the lattice thermal conductivity.

Thermal transport properties and *ZT* values

Fig. 5(a) shows the temperature-dependent total thermal conductivities of $Pb_{1.02}Se$, PbSe–0.2%Cu and $Pb_{1.02}Se$–0.2%Cu,

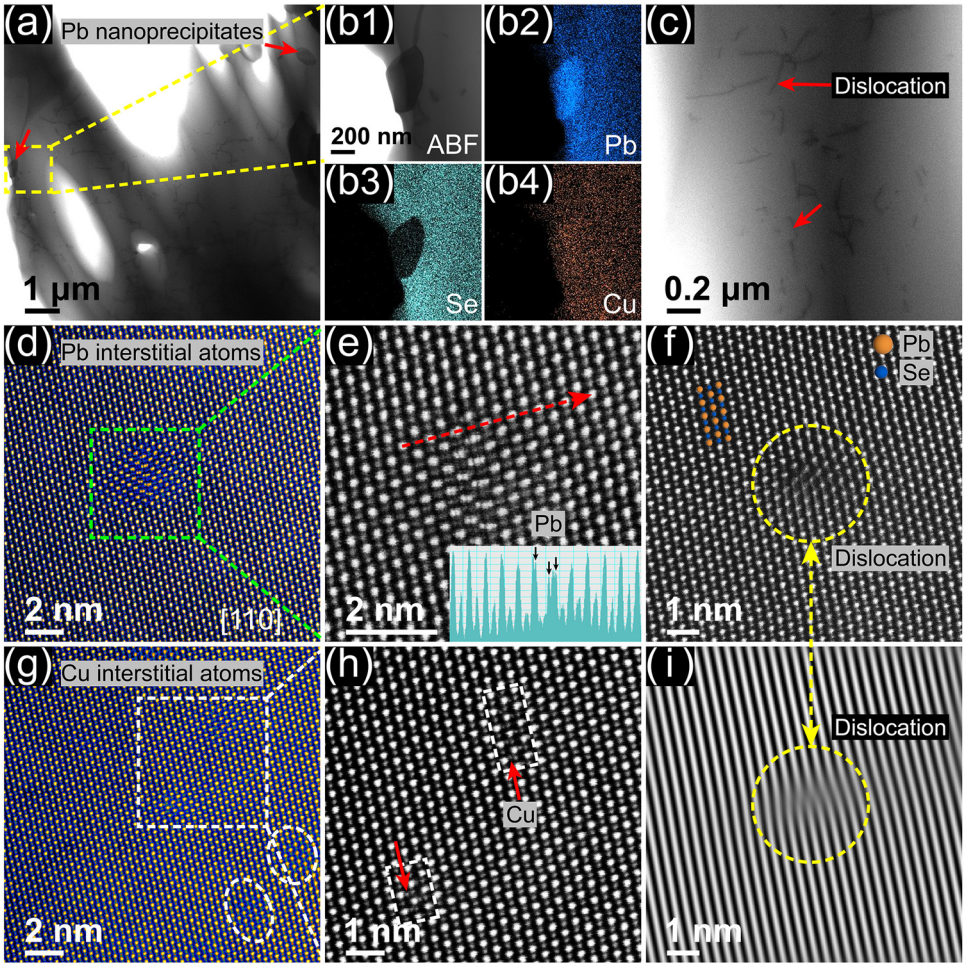

Fig. 4 The electron microscopic analysis of $Pb_{1.02}Se$–0.2%Cu: (a) the low magnification microscopic morphological ABF-STEM image; (b1)–(b4) a typical Pb nanoprecipitate and its corresponding elemental analysis; (c) the medium magnification ADF-STEM image showing many dislocations in the matrix as well as some tiny contrast belonging to the interstitial atoms; (d) atomic-scale HAADF-STEM image in the [110] axis, where some Pb interstitial atoms exist apparently; (e) the enlarged atomic image of (d) and the line profile in the inset image marked by the green dashed line; (f) a typical dislocation; (g) massive interstitial Cu atoms distributed in the PbSe matrix (marked by the white dashed box); (h) the magnified image of (g) shows a large number of obvious Cu interstitial atoms (marked by the white boxes); and (i) the corresponding FFT image of (f).

among which $Pb_{1.02}Se$ and $Pb_{1.02}Se$–0.2%Cu have parallel lower values. The low total thermal conductivity of $Pb_{1.02}Se$ originates from the low electronic thermal conductivity shown in Fig. S13(d) (ESI†), but the relatively low total thermal conductivity of $Pb_{1.02}Se$–0.2%Cu stems from the inferior lattice thermal conductivity shown in Fig. 5(b). The lattice thermal conductivity can be obtained by subtracting the electronic thermal conductivity from the total thermal conductivity, $\kappa_{lat} = \kappa_{tot} - \kappa_{ele}$, in which $\kappa_{ele} = L\sigma T$ based on the Wiedemann–Franz law, and the Lorenz number L is calculated from the experimental Seebeck coefficient according to the Single Parabolic Band (SPB) model, presented in Fig. S13(c) (ESI†). The comparatively lower lattice thermal conductivity of PbSe–0.2%Cu than that of $Pb_{1.02}Se$ indicates that Cu interstitials can more easily enter interstitial sites than Pb interstitials, which is consistent with the results of defect formation energy calculation in Fig. S9 (ESI†).[18] The further reduced lattice thermal conductivity of $Pb_{1.02}Se$–0.2%Cu compared with that of PbSe–0.2%Cu at high temperature could arise from the dynamic effect of Pb and Cu dual interstitial doping to promote phonon scattering.

To compare results of single Pb interstitial doping, single Cu interstitial doping and dual interstitial doping at 300–773 K, the temperature-dependent ratios of weighted carrier mobility to lattice thermal conductivity (μ_W/κ_{lat}) are calculated in Fig. 5(c). Obviously, the μ_W/κ_{lat} value of $Pb_{1.02}Se$–0.2%Cu surpasses those of $Pb_{1.02}Se$ and PbSe–0.2%Cu at 300–773 K, which demonstrates that Pb and Cu dual interstitial doping in PbSe is a valid method to simultaneously boost electrical and thermal transport properties over a wide range of temperatures. More detailed thermoelectric transport properties of $Pb_{1.02}Se$, PbSe–0.2%Cu and $Pb_{1.02}Se$–0.2%Cu can be found in Fig. S13 (ESI†). Finally, the temperature-dependent ZT values are further enhanced for $Pb_{1.02}Se$–0.2%Cu compared to those of single Pb or Cu interstitial doped PbSe samples, and the ZT_{RT} value enhances from 0.40 for $Pb_{1.02}Se$ and 0.37 for PbSe–0.2%Cu to 0.54 for $Pb_{1.02}Se$–0.2%Cu, as shown in Fig. 5(d). Such distinct

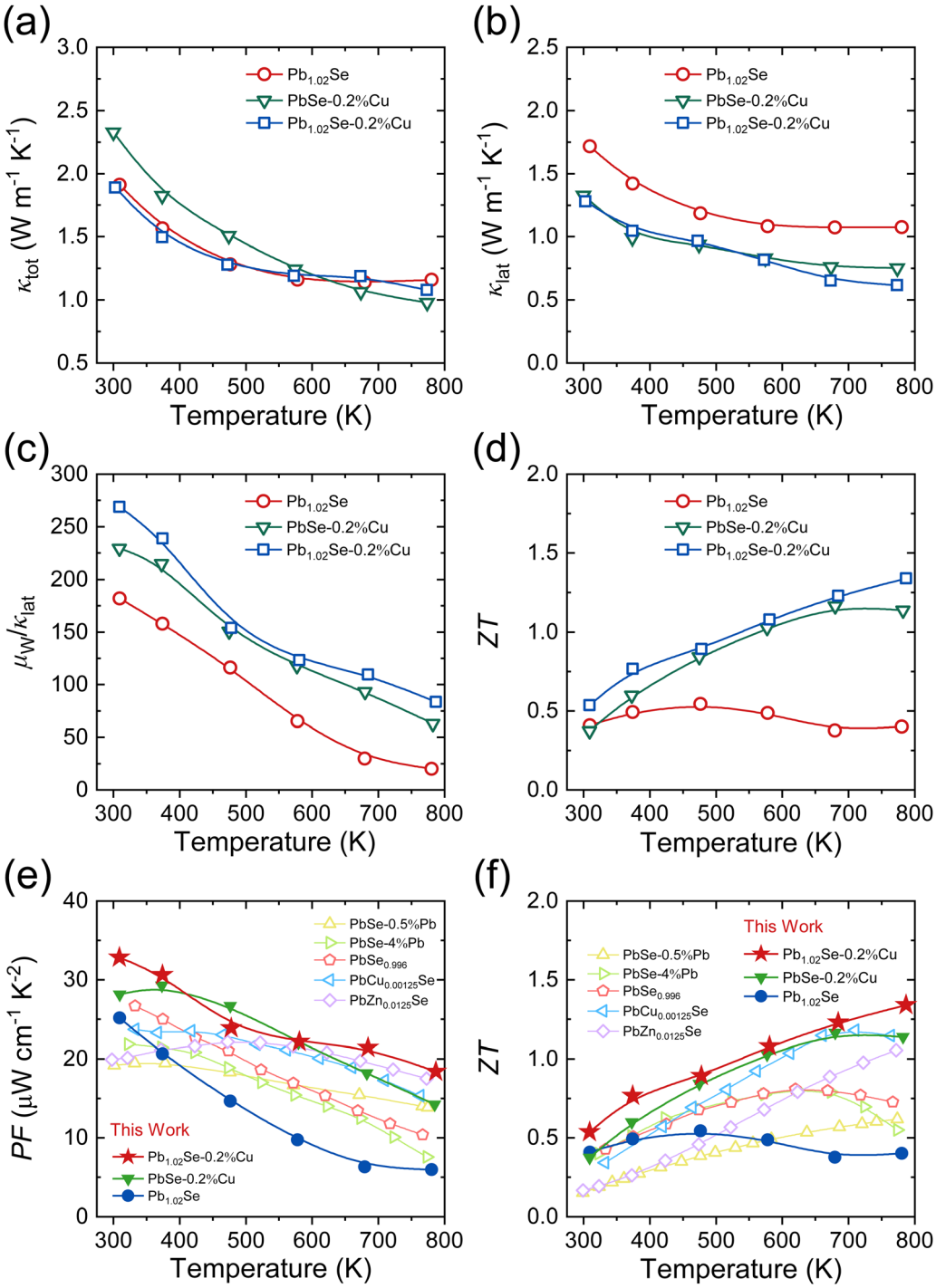

Fig. 5 Temperature-dependent thermal transport properties and *ZT* values of $Pb_{1.02}Se$, PbSe–0.2%Cu and $Pb_{1.02}Se$–0.2%Cu: (a) total thermal conductivity; (b) lattice thermal conductivity; (c) ratio of weighted carrier mobility to lattice thermal conductivity and (d) *ZT* values. Comparison of temperature-dependent thermoelectric properties of n-type PbSe with interstitial doping: (e) PF values and (f) *ZT* values.

enhancement of the *ZT* value at 300–773 K mainly benefits from the increased PF value. Compared with other single interstitial doped PbSe samples, such as $PbSe_{0.996}$,[39] $PbCu_{0.00125}Se$,[20] PbSe–4%Pb[38] and $PbZn_{0.0125}Se$,[16] $Pb_{1.02}Se$–0.2%Cu presents an optimal temperature-dependent PF value, as shown in Fig. 5(e), which contributes to a largely enhanced *ZT* value at 300–773 K presented in Fig. 5(f). The PF_{ave} value of 24.18 μW cm^{-1} K^{-2} and ZT_{ave} value of 1.01 at 300–773 K can be achieved for $Pb_{1.02}Se$–0.2%Cu, as shown in Fig. S14 (ESI†). Furthermore, the reproducible values further demonstrate the good thermoelectric reproducibility of $Pb_{1.02}Se$–0.2%Cu, and the cycle tests are provided to validate the long-term reliability

and practical feasibility of the dual interstitial doping strategy in practical applications, as shown in Fig. S15 and S16 (ESI†), respectively. The superior thermoelectric properties of $Pb_{1.02}Se$–0.2%Cu demonstrate that dual interstitial doping is a viable strategy to enhance the thermoelectric performance of lead chalcogenide thermoelectric materials over a wide range of temperatures.

Conclusions

In summary, both a high PF_{ave} of 24.18 μW cm^{-1} K^{-2} and a ZT_{ave} of 1.01 are achieved for a low-cost n-type $Pb_{1.02}Se$–0.2%Cu thermoelectric material at 300–773 K through Pb and Cu dual interstitial doping, which can simultaneously contribute to high output power and conversion efficiency. In addition, the high thermoelectric performance of n-type $Pb_{1.02}Se$–0.2%Cu not only surpasses those of other single interstitial doped PbSe thermoelectric materials, but also shows a strong competitive advantage over other cheap Se/S-based (Te free) n-type thermoelectric materials. Indeed, this work has proved the remarkable roles of the dual interstitial doping strategy in decoupling the carrier and phonon transport properties of thermoelectric materials, including (1) dynamically tuned carrier density to maximize the power factor over a wide range of temperatures and (2) electron-dominated defect regions to maintain carrier transport and simultaneously impede phonon propagation to largely reduce the lattice thermal conductivity. This work proves the feasibility of dual interstitials in effectively decoupling carrier and phonon transport, and more strategies of dual or multiple interstitial doping are worthy of being explored as universal methods to be extended to other thermoelectric materials.

Author contributions

Yu Xiao and Liqing Xu designed the experiment, synthesized the samples, carried out the transport property measurements and wrote the manuscript. Xiaoying Wang, Yang Wang and Zhibin Gao performed the DFT calculations. Xiangdong Ding and Yu Xiao discussed the results and revised this manuscript.

Conflicts of interest

The authors declare no conflict of interest.

Acknowledgements

The authors acknowledge the financial support from the National Natural Science Foundation of China, Grant No. 52172236 and the fund of the State Key Laboratory of Solidification Processing in NPU, Grant No. SKLSP202314. Z. Gao acknowledges the support from the National Natural Science Foundation of China (No. 12104356 and 52250191), the Opening Project of Shanghai Key Laboratory of Special Artificial Microstructure Materials and Technology (Ammt2022B-1), and the Fundamental Research Funds for the Central Universities. Y. Xiao would like to acknowledge the support from the ''Bairen'' Program of University of Electronic Science and Technology of China and the help from Prof. Z. Luo and Dr Z. Chen of Fuzhou university for the carrier density analysis.

References

1 C. Chang, B. Qin, L. Su and L.-D. Zhao, *Sci. Bull.*, 2022, **67**, 1105–1107.
2 X. Tang, Z. Li, W. Liu, Q. Zhang and C. Uher, *Interdiscip. Mater.*, 2022, **1**, 88–115.
3 H. Pang, X. Zhang, D. Wang, R. Huang, Z. Yang, X. Zhang, Y. Qiu and L.-D. Zhao, *J. Materiomics*, 2022, **8**, 184–194.
4 W. Liu, H. S. Kim, S. Chen, Q. Jie, B. Lv, M. Yao, Z. Ren, C. P. Opeil, S. Wilson, C. W. Chu and Z. Ren, *Proc. Natl. Acad. Sci. U. S. A.*, 2015, **112**, 3269–3274.
5 Q. H. Zhang, X. Y. Huang, S. Q. Bai, X. Shi, C. Uher and L. D. Chen, *Adv. Eng. Mater.*, 2015, **18**, 194–213.
6 B. Jiang, Y. Yu, J. Cui, X. Liu, L. Xie, J. Liao, Q. Zhang, Y. Huang, S. Ning, B. Jia, B. Zhu, S. Bai, L. Chen, S. Pennycook and J. He, *Science*, 2021, **371**, 830–834.
7 B. Jiang, W. Wang, S. Liu, Y. Wang, C. Wang, Y. Chen, L. Xie, M. Huang and J. He, *Science*, 2022, **377**, 208–213.
8 Y. Xiao, L. Xu, T. Hong, H. Shi, S. Wang, X. Gao, X. Ding, J. Sun and L.-D. Zhao, *Energy Environ. Sci.*, 2022, **15**, 346–355.
9 T. Chasapis, Y. Lee, E. Hatzikraniotis, K. Paraskevopoulos, H. Chi, C. Uher and M. Kanatzidis, *Phys. Rev. B: Condens. Matter Mater. Phys.*, 2015, **91**, 085207.
10 Z. Chen, H. Cui, S. Hao, Y. Liu, H. Liu, J. Zhou, Y. Yu, Q. Yan, C. Wolverton, V. Dravid, Z. Luo, Z. Zou and M. Kanatzidis, *Energy Environ. Sci.*, 2023, **16**, 1676–1684.
11 L. Xu, Y. Xiao, S. Wang, B. Cui, D. Wu, X. Ding and L.-D. Zhao, *Nat. Commun.*, 2022, **13**, 6449.
12 Z. Chen, B. Ge, W. Li, S. Lin, J. Shen, Y. Chang, R. Hanus, G. J. Snyder and Y. Pei, *Nat. Commun.*, 2017, **8**, 13828.
13 S. Cai, S. Hao, Z. Luo, X. Li, I. Hadar, T. Bailey, X. Hu, C. Uher, Y. Hu, C. Wolverton, V. Dravid and M. Kanatzidis, *Energy Environ. Sci.*, 2020, **13**, 200–211.
14 Y. Qin, Y. Xiao and L.-D. Zhao, *APL Mater.*, 2020, **8**, 010901.
15 Y. Xiao, H. Wu, W. Li, M. Yin, Y. Pei, Y. Zhang, L. Fu, Y. Chen, S. Pennycook, L. Huang, J. He and L.-D. Zhao, *J. Am. Chem. Soc.*, 2017, **139**, 18732–18738.
16 X. Qian, H. Wu, D. Wang, Y. Zhang, S. Pennycook, X. Gao, L. Zheng and L.-D. Zhao, *Mater. Today Phys.*, 2019, **9**, 100102.
17 Z. Hou, T. Hong, D. Wang, X. Gao, Y. Qiu and L.-D. Zhao, *ACS Appl. Energy Mater.*, 2021, **4**, 6284–6289.
18 X. Qian, D. Wang, Y. Zhang, H. Wu, S. Pennycook, L. Zheng, P. Poudeu and L.-D. Zhao, *J. Mater. Chem. A*, 2020, **8**, 5699–5708.
19 Y. Xiao, Y. Wu, P. Nan, H. Dong, Z. Chen, Z. Chen, H. Gu, B. Ge, W. Li and Y. Pei, *Chem*, 2020, **6**, 523–537.
20 L. You, Y. Liu, X. Li, P. Nan, B. Ge, Y. Jiang, P. Luo, S. Pan, Y. Pei, W. Zhang, G. Snyder, J. Yang, J. Zhang and J. Luo, *Energy Environ. Sci.*, 2018, **11**, 1848–1858.

21 Z. Hou, D. Wang, T. Hong, Y. Qin, S. Peng, G. Wang, J. Wang, X. Gao, Z. Huang and L.-D. Zhao, *J. Phys. Chem. Solids*, 2021, **148**, 109640.
22 S. Wang, C. Chang, S. Bai, B. Qin, Y. Zhu, S. Zhan, J. Zheng, S. Tang and L.-D. Zhao, *Chem. Mater.*, 2023, **35**, 755–763.
23 W. Li, J. Wang, Y. Xie, J. Gray, J. Heremans, H. B. Kang, B. Poudel, S. Huxtable and S. Priya, *Chem. Mater.*, 2019, **31**, 862–872.
24 W. Zhao, P. Wei, Q. Zhang, H. Peng, W. Zhu, D. Tang, J. Yu, H. Zhou, Z. Liu, X. Mu, D. He, J. Li, C. Wang, X. Tang and J. Yang, *Nat. Commun.*, 2015, **6**, 6197.
25 Y. Tang, R. Hanus, S. Chen and G. Snyder, *Nat. Commun.*, 2015, **6**, 7584.
26 B. Ortiz, C. Crawford, R. McKinney, P. Parilla and E. Toberer, *J. Mater. Chem. A*, 2016, **4**, 8444–8450.
27 W. Ren, H. Zhu, J. Mao, L. You, S. Song, T. Tong, J. Bao, J. Luo, Z. Wang and Z. Ren, *Adv. Electron. Mater.*, 2019, **5**, 1900166.
28 S. A. Barczak, J. Buckman, R. I. Smith, A. R. Baker, E. Don, I. Forbes and J. G. Bos, *Materials*, 2018, **11**, 536.
29 S. Barczak, J. Halpin, J. Buckman, R. Decourt, M. Pollet, R. Smith, D. MacLaren and J. Bos, *ACS Appl. Mater. Interfaces*, 2018, **10**, 4786–4793.
30 C. Kim, D. H. Lopez, D. H. Kim and H. Kim, *J. Mater. Chem. A*, 2019, **7**, 791–800.
31 J. Guo, Z. Wang, Y. Zhu, L. Chen, J. Feng and Z. Ge, *Rare Met.*, 2021, **41**, 931–941.
32 N. Arshad, N. Abbas and A. Ali, *J. Nanopart. Res.*, 2022, **24**, 223.
33 W. Liu, Q. Zhang, Y. Lan, S. Chen, X. Yan, Q. Zhang, H. Wang, D. Wang, G. Chen and Z. Ren, *Adv. Energy Mater.*, 2011, **1**, 577–587.
34 L. Li, P. Wei, M. Yang, W. Zhu, X. Nie, W. Zhao and Q. Zhang, *Sci. China Mater.*, 2023, **66**, 3651–3658.
35 J. Wang, X. Jia, S. Lou, G. Li and S. Zhou, *ACS Omega*, 2020, **5**, 12409–12414.
36 C. Zhou, Y. Yu, X. Zhang, Y. Cheng, J. Xu, Y. Lee, B. Yoo, O. Cojocaru-Mirédin, G. Liu, S. P. Cho, M. Wuttig, T. Hyeon and I. Chung, *Adv. Funct. Mater.*, 2019, **30**, 1908405.
37 C. Liu, Z. Huang, D. Wang, X. Wang, L. Miao, X. Wang, S. Wu, N. Toyama, T. Asaka, J. Chen, E. Nishibori and L.-D. Zhao, *J. Mater. Chem. A*, 2019, **7**, 9761–9772.
38 C. Wu, T. Wei and J. Li, *APL Mater.*, 2016, **4**, 104801.
39 Y. Liu, L. You, C. Wang, J. Zhang, J. Yang, K. Guo, J. Luo and W. Zhang, *J. Electron. Mater.*, 2018, **47**, 2584–2590.
40 C. Chang, M. Wu, D. He, Y. Pei, C. Wu, X. Wu, H. Yu, F. Zhu, K. Wang, Y. Chen, L. Huang, J.-F. Li, J. He and L.-D. Zhao, *Science*, 2018, **360**, 778–783.
41 L. Mao, Y. Yin, Q. Zhang, G. Liu, H. Wang, Z. Guo, H. Hu, Y. Xiao, X. Tan and J. Jiang, *Energy Environ. Sci.*, 2020, **13**, 616–621.
42 S. Zhan, T. Hong, B. Qin, Y. Zhu, X. Feng, L. Su, H. Shi, H. Liang, Q. Zhang, X. Gao, Z. H. Ge, L. Zheng, D. Wang and L. D. Zhao, *Nat. Commun.*, 2022, **13**, 5937.
43 C. Zhou, Y. Yu, Y. K. Lee, O. Cojocaru-Miredin, B. Yoo, S. P. Cho, J. Im, M. Wuttig, T. Hyeon and I. Chung, *J. Am. Chem. Soc.*, 2018, **140**, 15535–15545.
44 Z. Liu, T. Hong, L. Xu, S. Wang, X. Gao, C. Chang, X. Ding, Y. Xiao and L.-D. Zhao, *Interdiscip. Mater.*, 2022, **2**, 161–170.
45 H. Shi, L. Su, S. Bai, B. Qin, Y. Wang, S. Liu, C. Chang and L.-D. Zhao, *Energy Environ. Sci.*, 2023, **16**, 3128–3136.
46 S. Chandra, U. Bhat, P. Dutta, A. Bhardwaj, R. Datta and K. Biswas, *Adv. Mater.*, 2022, **34**, e2203725.
47 Y. Wei, J. Li, D. Zhang, B. Zhang, Z. Zhou, G. Han, G. Wang, C. Prestipino, P. Lemoine, E. Guilmeau, X. Lu and X. Zhou, *Acta Mater.*, 2024, **263**, 119504.
48 Y. Luo, Y. Zheng, Z. Luo, S. Hao, C. Du, Q. Liang, Z. Li, K. A. Khor, K. Hippalgaonkar, J. Xu, Q. Yan, C. Wolverton and M. G. Kanatzidis, *Adv. Energy Mater.*, 2017, **8**, 1702167.
49 W. He, T. Hong, D. Wang, X. Gao and L.-D. Zhao, *Sci. China Mater.*, 2021, **64**, 3051–3058.
50 M. Samanta, K. Pal, P. Pal, U. V. Waghmare and K. Biswas, *J. Am. Chem. Soc.*, 2018, **140**, 5866–5872.
51 S. Wang, Y. Sun, J. Yang, B. Duan, L. Wu, W. Zhang and J. Yang, *Energy Environ. Sci.*, 2016, **9**, 3436–3447.
52 X. Liu, D. Wang, H. Wu, J. Wang, Y. Zhang, G. Wang, S. J. Pennycook and L. D. Zhao, *Adv. Funct. Mater.*, 2018, **29**, 1806558.
53 K. Jin, J. Tiwari, T. Feng, Y. Lou and B. Xu, *Nano Energy*, 2022, **100**, 107478.
54 Y. Gu, K. Song, X. Hu, C. Chen, L. Pan, C. Lu, X. Shen, K. Koumoto and Y. Wang, *ACS Appl. Mater. Interfaces*, 2020, **12**, 41687–41695.
55 L. You, J. Zhang, S. Pan, Y. Jiang, K. Wang, J. Yang, Y. Pei, Q. Zhu, M. Agne, G. Snyder, Z. Ren, W. Zhang and J. Luo, *Energy Environ. Sci.*, 2019, **12**, 3089–3098.
56 Y. Ravich, B. Efimova and I. Smirnov, *Semiconducting Lead Chalcogenides*, Plenum Press, New York, 1970.
57 Y. Ravich, B. Efimova and V. Tamarchenko, *Phys. Status Solidi B*, 1971, **43**, 453–469.
58 H. Wang, Y. Pei, A. D. LaLonde and G. J. Snyder, *Proc. Natl. Acad. Sci. U. S. A.*, 2012, **109**, 9705–9709.
59 B. Silvi and A. Savin, *Nature*, 1994, **371**, 683–686.
60 Z. Liu, W. Zhang, W. Gao and T. Mori, *Energy Environ. Sci.*, 2021, **14**, 3579–3587.
61 A. Savin, O. Jepsen, J. Flad, O. K. Andersen, H. Preuss and H. Schnering, *Angew. Chem., Int. Ed. Engl.*, 1992, **31**, 187–188.